molecules

MDPI

Article

Characterization on Lead-Free Hybrid Perovskite $[NH_3(CH_2)_5NH_3]CuCl_4$: Thermodynamic Properties and Molecular Dynamics

Ae Ran Lim [1,2,*] and Sang Hyeon Park [1]

[1] Graduate School of Carbon Convergence Engineering, Jeonju University, Jeonju 55069, Korea; klly89@naver.com
[2] Department of Science Education, Jeonju University, Jeonju 55069, Korea
* Correspondence: aeranlim@hanmail.net or arlim@jj.ac.kr; Tel.: +82-(0)63-220-2514

Abstract: It is essential to develop novel zero- and two-dimensional hybrid perovskites to facilitate the development of eco-friendly solar cells. In this study, we investigated the structure and dynamics of $[NH_3(CH_2)_5NH_3]CuCl_4$ via various characterization techniques. Nuclear magnetic resonance (NMR) results indicated that the crystallographic environments of ^1H in NH_3 and ^{13}C on C3, located close to NH_3 at both ends of the cation, were changed, indicating a large structural change of $CuCl_6$ connected to N–H···Cl. The thermal properties and structural dynamics of the $[NH_3(CH_2)_nNH_3]$ cation in $[NH_3(CH_2)_nNH_3]CuCl_4$ (n = 2, 3, 4, and 5) crystals were compared using thermogravimetric analysis (TGA) and NMR results for the methylene chain. The ^1H and ^{13}C spin-lattice relaxation times ($T_{1\rho}$) exhibited similar trends upon the variation of the methylene chain length, with n = 2 exhibiting shorter $T_{1\rho}$ values than n = 3, 4, and 5. The difference in $T_{1\rho}$ values was related to the length of the cation, and the shorter chain length (n = 2) exhibited a shorter $T_{1\rho}$ owing to the one closest to the paramagnetic Cu^{2+} ions.

Keywords: organic-inorganic hybrid; perovskite; ferroelasticity; nuclear magnetic resonance; thermodynamic properties

check for updates

Citation: Lim, A.R.; Park, S.H. Characterization on Lead-Free Hybrid Perovskite $[NH_3(CH_2)_5NH_3]CuCl_4$: Thermodynamic Properties and Molecular Dynamics. *Molecules* **2022**, *27*, 4546. https://doi.org/10.3390/molecules27144546

Academic Editor: Danilo Roccatano

Received: 20 June 2022
Accepted: 15 July 2022
Published: 16 July 2022

Publisher's Note: MDPI stays neutral with regard to jurisdictional claims in published maps and institutional affiliations.

Copyright: © 2022 by the authors. Licensee MDPI, Basel, Switzerland. This article is an open access article distributed under the terms and conditions of the Creative Commons Attribution (CC BY) license (https://creativecommons.org/licenses/by/4.0/).

1. Introduction

Recently, research on solar cells based on organic-inorganic hybrid materials has progressed very rapidly [1–4]. Initially, $CH_3NH_3PbX_3$ (X = Cl, Br, I)-based thin-film photovoltaic devices were used as solar cells. Despite the development of $CH_3NH_3PbX_3$ as a hybrid solar cell, it readily decomposes in humid air, and Pb toxicity is a major concern [5–7]. Therefore, its replacement with environment-friendly hybrid perovskite solar cells is vital.

Further, novel groups of perovskite materials, such as $[(CH_3)_2NH_2]Zn(HCOO)_3$, consisting of an organic cation and a metal ion, have been discussed [8–14]. They exhibited potential for application in memory manipulation devices and next-generation memory storage technology. In addition, it is necessary to study the structure and dynamics of new materials with zero- and two-dimensional (2D) hybrid perovskites, such as eco-friendly $[NH_3(CH_2)_nNH_3]MX_4$. The organic-inorganic hybrid $[NH_3(CH_2)_nNH_3]MX_4$ (n = 2, 3, 4, ···), where M is a divalent metal ion, and X is a halide ion, crystallizes in perovskite-type layered structures [15–31]. The organic $[NH_3(CH_2)_nNH_3]$ cation of the hybrid complex influences properties, such as structural flexibility and optical characteristics, whereas the inorganic (MX_4 or MX_6) anions affect the thermal and mechanical properties [32,33]. For M = Mn, Cu, or Cd, the structure consists of the corner shared octahedral $(MX_6)^{2-}$ alternated with organic layers and is 2-dimensional, while for M = Co or Zn, the structures are tetrahedral $(MX_4)^{2-}$ sandwiched between layers of organic cations and 0-dimensional. The ammonium ions at the organic-cation terminals form N−H···X

hydrogen bonds with halide ions of the metallic inorganic layer [34–36]. For long chains, in complexes where n is 5 or more, structural changes due to conformational changes of the chains are important [37]. Among them, an interesting group of hybrid materials is perovskite-type layered $[NH_3(CH_2)_5NH_3]CuCl_4$. Its crystal structure consists of 2D inorganic $CuCl_4$ layers and 1,5-diaminopentane cations. The $[NH_3(CH_2)_5NH_3]$ organic chains exhibit the longest c-axis. $[NH_3(CH_2)_5NH_3]CuCl_4$ crystallizes in the monoclinic space group $P2_1/c$, with unit-cell parameters of a = 7.747 Å, b = 7.203 Å, c = 21.512 Å, Z = 4, and β = 98.48° [38].

Filloleau et al. [39] and Kanel et al. [40] reported the magnetic, optical properties, and electron paramagnetic resonance studies of $[NH_3(CH_2)_5NH_3]CuCl_4$ crystals. Recently, the thermal properties and structural molecular dynamics of $[NH_3(CH_2)_nNH_3]CuCl_4$ (n = 2, 3, and 4) crystals containing Cu^{2+} ions have been reported [41–43]. However, a detailed report on the $[NH_3(CH_2)_5NH_3]CuCl_4$ crystal is yet to be published. A lot of research has been done on the electric and conductive properties of this type of compound [44–47].

In this study, the crystal structure, thermodynamics, and ferroelasticity of $[NH_3(CH_2)_5NH_3]CuCl_4$ were studied to investigate the $CuCl_6$ anion, which is responsible for the thermal and mechanical properties. Additionally, to obtain information on the coordination geometry and molecular dynamics of the $[NH_3(CH_2)_5NH_3]$ cation, nuclear magnetic resonance (NMR) chemical shifts and spin-lattice relaxation times ($T_{1\rho}$) for ^1H and ^{13}C were measured using the magic angle spinning (MAS) method. The variations in physicochemical properties of this crystal according to the temperature change were explained by considering the cation and the $CuCl_4$ anion. The influence of the CH_2-group length in the $[NH_3(CH_2)_nNH_3]$ cation of $[NH_3(CH_2)_nNH_3]CuCl_4$ (n = 2, 3, 4, and 5) has also been discussed with reference to a previous report. These results, which consider the methylene chain length, could be useful for facilitating diverse environment-friendly applications in the future.

2. Results

2.1. Crystal Structure

The X-ray diffraction (XRD) powder patterns of the $[NH_3(CH_2)_5NH_3]CuCl_4$ crystal were obtained at different temperatures during heating, and the results are shown in Figure 1. The XRD patterns from 300 K to 440 K were identical, and the XRD patterns at temperatures above 440 K were due to the melting of the crystal. Additionally, the crystal structure is monoclinic, and the lattice constants, analyzed from the single-crystal XRD results, were a = 7.7385 Å, b = 7.2010 Å, c = 21.5308 Å, β = 98.493°, and Z = 4, with the space group $P2_1/c$. This result is consistent with a previous report [38].

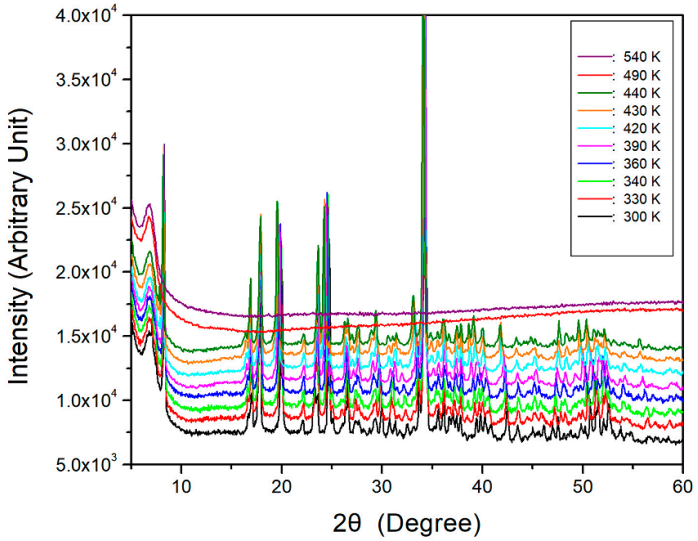

Figure 1. XRD powder patterns of the $[NH_3(CH_2)_5NH_3]CuCl_4$ crystal at different temperatures.

2.2. Thermal Property and Ferroelastic Twin Domain

To understand the thermodynamic properties, thermogravimetric analysis (TGA) and differential thermal analysis (DTA) results measured at a heating rate of 10 K/min are shown in Figure 2. The first occurrence of molecular weight loss, indicating the initiation of partial thermal decomposition, occurred at approximately 514 K. As the temperature increased, the molecular weight of the $[NH_3(CH_2)_5NH_3]CuCl_4$ crystal decreased. TGA results of a similar compound were reported by another group previously [24,27,48]. The 12% and 24% losses, calculated from the total molecular weight, were caused by the decomposition of HCl and 2HCl, respectively. The temperatures of HCl and 2HCl loss obtained by TGA were 531 and 583 K, respectively, with a weight loss of 80% at ~900 K. The molecular weight sharply decreased between 520 and 650 K, with a corresponding weight loss of 70% at ~650 K. Subsequently, the crystals were analyzed using optical polarizing microscopy experiments with increasing temperature to investigate their thermal stability. The crystals were yellow at room temperature, as shown in the inset of Figure 2. As the temperature increased, the crystals changed from yellow to light brown and finally to dark brown, above 490 K, consistent with that shown in the XRD powder patterns of Figure 1. The possibility to change color was due to decomposition by loss of HCl and also due to the geometrical change of $CuCl_4$. Near 540 K, the single-crystal surfaces exhibited slight melting. This temperature was similar to the temperature of HCl loss in the TGA experiment. Additionally, no endothermic peak corresponding to a phase transition above 200 K was observed in the differential scanning calorimetry (DSC) curve.

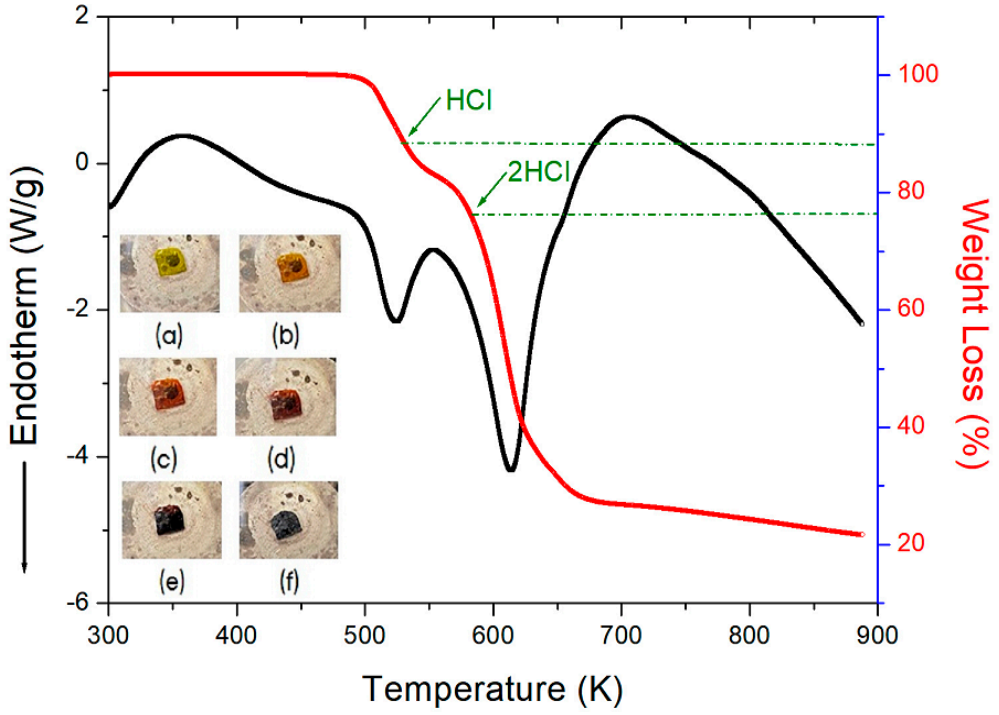

Figure 2. TGA and DTA curves of $[NH_3(CH_2)_5NH_3]CuCl_4$ (inset: changes in the crystal at the following temperatures: (**a**) 300 K, (**b**) 330 K, (**c**) 390 K, (**d**) 430 K, (**e**) 490 K, and (**f**) 540 K).

A single crystal with ferroelastic properties has two or more orientation states, even in the absence of mechanical stress, and changes from one orientation state to another under mechanical stress [49,50]. The domain patterns observed under a polarized optical microscope are shown in Figure 3. One of the most common microstructures is related to twinning, with dominant twin planes oriented nearly perpendicular to each other. Ferroelastic domain patterns, represented by parallel lines, were observed at room temperature (Figure 3a). Although the crystal color changed with an increase in temperature, the twin domain patterns remained unchanged. Finally, the domain pattern turned dark brown

near 440 K, as shown in Figure 3f, making it difficult to observe. The difficulty in observing the domain pattern above 440 K was due to the phenomenon in which single crystals begin to melt.

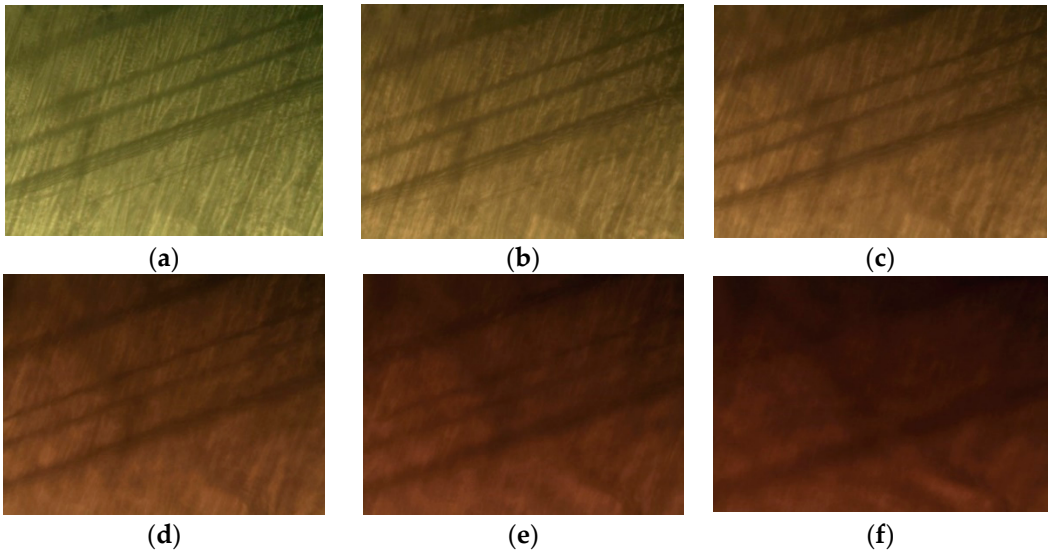

Figure 3. Optical polarizing microscopy images of $[NH_3(CH_2)_5NH_3]CuCl_4$ at (**a**) 300 K, (**b**) 340 K, (**c**) 360 K, (**d**) 390 K, (**e**) 420 K, and (**f**) 440 K. Parallel lines represent ferroelastic twin domain walls.

2.3. ^1H NMR Chemical Shifts

The temperature dependence of the ^1H MAS NMR spectra of the $[NH_3(CH_2)_5NH_3]CuCl_4$ crystal was analyzed, and the ^1H chemical shifts are shown in Figure 4. In the $[NH_3(CH_2)_5NH_3]$ cation, the number of protons related to NH_3 and CH_2 was 6 and 10, respectively, and the intensity and linewidth of the ^1H resonance peak were also related to the number of protons. The ^1H signal in NH_3 was observed at low temperatures, whereas the ^1H signal in CH_2 was difficult to observe, owing to its wide linewidth. Above 240 K, the NMR spectrum featured two resonance lines of NH_3 and CH_2. At 300 K, the ^1H chemical shifts in NH_3 and CH_2 were 12.11 and 2.89 ppm, respectively. ^1H signals for NH_3 and CH_2 overlap each other. Thus, their line widths could not be accurately distinguished in accordance with the temperature change; however, the line width of NH_3 was narrower than that of CH_2. The spinning sidebands for NH_3 and CH_2 are marked with open circles and crosses, respectively. The ^1H chemical shifts of CH_2, indicated by dotted lines in Figure 4, were almost independent of temperature.

The ^1H chemical shift for NH_3, from 180–220 K, was in the negative direction but shifted slightly in the negative direction at temperatures above that. Therefore, the structural environment of ^1H in NH_3 changed with the variation of temperature, while the environment of ^1H in CH_2 changed negligibly.

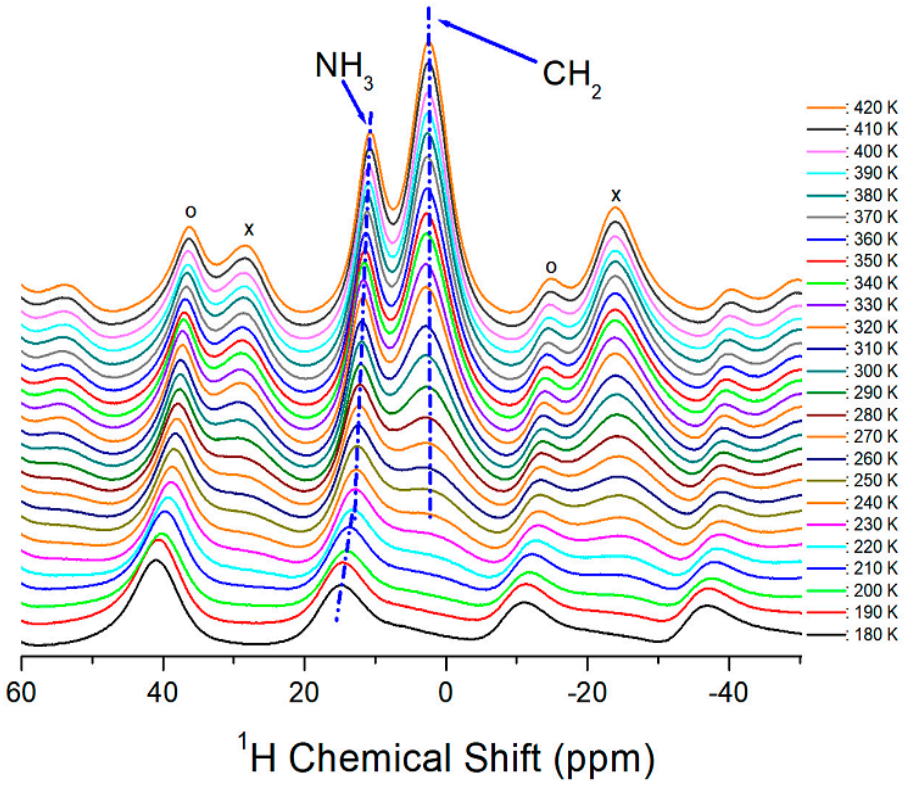

Figure 4. MAS ^{1}H NMR spectra of $[NH_3(CH_2)_5NH_3]CuCl_4$ as a function of temperature. Spinning sidebands are indicated by crosses and open circles.

2.4. ^{13}C NMR Chemical Shifts

^{13}C chemical shifts for the in-situ MAS NMR spectra with increasing temperature are shown in Figure 5. The tetramethylsilane (TMS) reference signal was recorded at 38.3 ppm at 300 K and considered to be the ^{13}C chemical-shift standard. In the $[NH_3(CH_2)_5NH_3]$ cation, the CH_2 close to NH_3 was labeled C3. The CH_2 at the center of the cation was labeled C1, and the CH_2 between C3 and C1 was labeled C2, as shown in the inset of Figure 5. At 300 K, the ^{13}C chemical shifts were recorded at 27.19, 50.94, 62.95, and 118.46 ppm for C1, C22, C22′, and C3, respectively. The ^{13}C chemical shifts for C1, C2, and C3, with temperature changes, are shown in Figure 5. The chemical shifts of C3 shifted rapidly in the negative direction with temperature change, while C1 shifted in a slightly positive direction. However, there were two different signals (C22 and C22′) for C2. Here, the chemical shift of C22 shifted in a negative direction, while that of C22′ shifted in a slightly positive direction, with a temperature change. The shifting of C22 and C22′ chemical shifts in different directions could be because of the position of C1 at the center of the cation and that of C2 between C1 and C3. In addition, at higher temperatures, the line widths for C1, C2, and C3, as shown in the inset of Figure 5, narrowed significantly owing to high internal mobility [51]. All ^{13}C chemical shifts changed with the increase in temperature, with the C3 chemical shift exhibiting a rapid change.

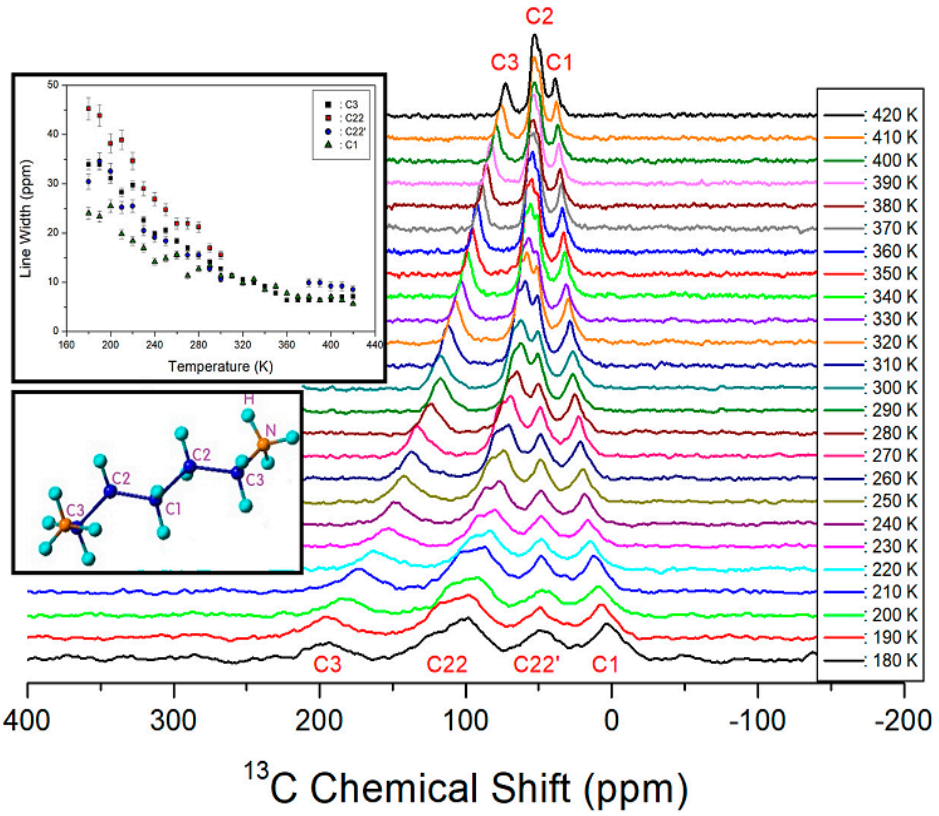

Figure 5. MAS ^{13}C NMR spectra of $[NH_3(CH_2)_5NH_3]CuCl_4$ as a function of temperature.

2.5. ^{1}H and ^{13}C Spin-Lattice Relaxation Times

The intensities of the ^{1}H MAS NMR and ^{13}C MAS NMR spectra were measured by changing delay times at each temperature. The spectral intensity versus the delay time plot followed a mono-exponential function. The recovery traces of magnetization were characterized by the spin-lattice relaxation time, $T_{1\rho}$, as [52–54]:

$$P_{H(C)}(\tau) = P_{H(C)}(0)\exp(-\tau/T_{1\rho}) \quad (1)$$

where $P_{H(C)}(\tau)$ and $P_{H(C)}(0)$ are signal intensities for the proton (carbon) at time τ and $\tau = 0$, respectively. From the slope of the logarithm of intensity versus the delay time plot, the ^{1}H $T_{1\rho}$ values were determined for NH_3 and CH_2 at several temperatures. The intensity of each signal differed with the delay time. The results of ^{1}H $T_{1\rho}$ obtained here and the ^{1}H $T_{1\rho}$ of n = 2, 3, and 4 previously reported are shown in Figure 6 as a function of the inverse temperature. The ^{1}H $T_{1\rho}$ values were almost temperature independent and were in the order of 10 ms. However, the ^{1}H $T_{1\rho}$ values of NH_3, represented with black squares, were shorter than those of CH_2, marked with black open squares. Here, the $T_{1\rho}$ values were compared according to the cation length from n = 2–5. The ^{1}H $T_{1\rho}$ values exhibited similar trends for different methylene chain lengths, with n = 2 exhibiting slightly shorter values than n = 3, 4, and 5.

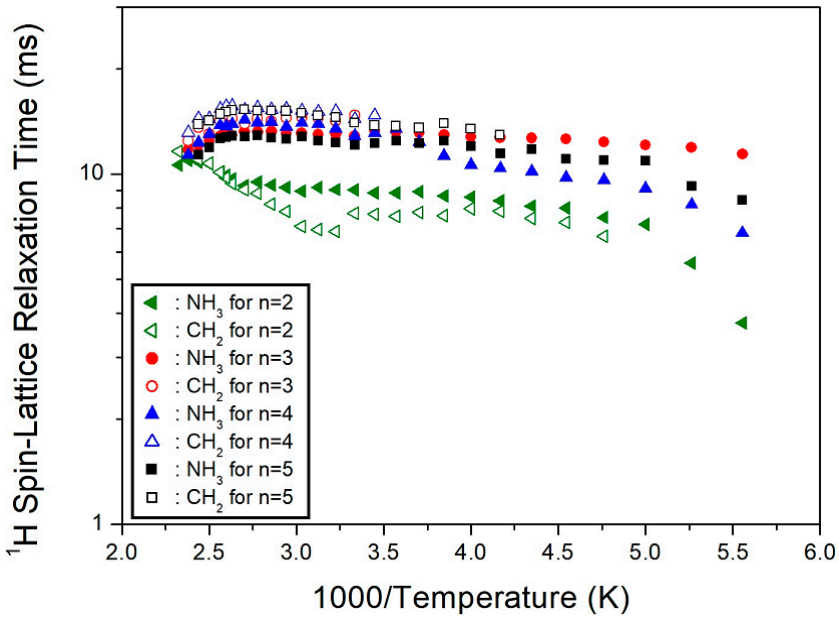

Figure 6. Temperature dependence of ^{1}H NMR spin-lattice relaxation times ($T_{1\rho}$) in $[NH_3(CH_2)_nNH_3]CuCl_4$ (n = 2, 3, 4, and 5).

The ^{13}C $T_{1\rho}$ values for C1, C2, and C3 were obtained as a function of the inverse temperature from the slope of the logarithm of intensity versus the delay time plot (Figure 7). The ^{13}C $T_{1\rho}$ values increased rapidly from 10–100 ms. The $T_{1\rho}$ behavior for random motions, with a correlation time τ_C, could be elucidated by a fast motion. The $T_{1\rho}$ value of C3, located close to the paramagnetic Cu^{2+} ion, was shorter than that of C2, located further away from Cu^{2+}. Additionally, the $T_{1\rho}$ of C1, at the center of 5 CH_2, exhibited very short values. It is interesting to compare the results for ^{13}C $T_{1\rho}$ according to the alkyl chain lengths. In the $[NH_3(CH_2)_nNH_3]$ cation, the marks of C1, C2, and C3 along the length of n are shown in Figure 8. The ^{13}C $T_{1\rho}$ values exhibited similar trends for n =3, 4, and 5, with a very short value for n = 2, as shown in Figure 7. In the case of n = 5, unlike n = 2, 3, and 4, the $T_{1\rho}$ value of C2 was different from those of C1 and C3. Overall, energy transfer was easier for the short alkyl chain length (n = 2).

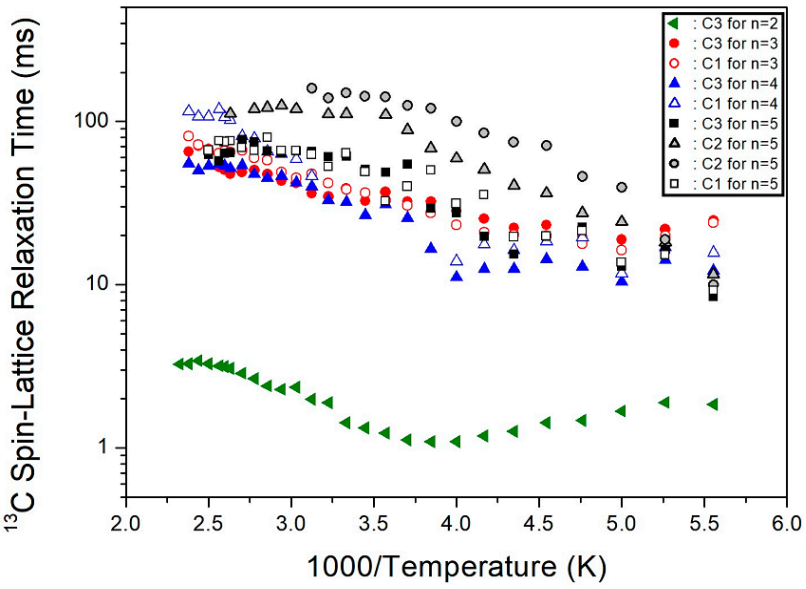

Figure 7. Temperature dependence of ^{13}C NMR spin-lattice relaxation times ($T_{1\rho}$) in $[NH_3(CH_2)_nNH_3]CuCl_4$ (n = 2, 3, 4, and 5).

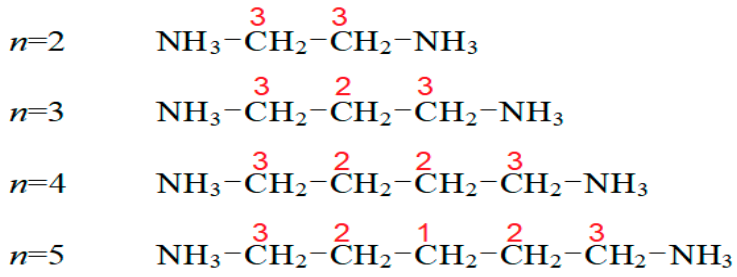

Figure 8. Names of carbons, according to their length, in the cation structure of $[NH_3(CH_2)_nNH_3]CuCl_4$. (n = 2, 3, 4, and 5).

3. Discussion

The thermal properties and structural dynamics of the $[NH_3(CH_2)_nNH_3]$ cation in $[NH_3(CH_2)_nNH_3]CuCl_4$ (n = 2, 3, 4, and 5) crystals were analyzed and compared using information obtained from TGA and NMR experiments. Thermal decomposition temperatures (T_d) decreased with an increase in the value of n, as observed in the TGA results of the four crystals. An enlarged view was observed near T_d; for n = 2, 3, 4, and 5, T_d values, when the case of 5% weight loss was set as T_d, were 533, 530, 527, and 514 K, respectively, indicating no improvement in thermal stability with an increase in the cation length (Figure 9). The ^1H and ^{13}C $T_{1\rho}$ values exhibited a similar trend in increasing the methylene chain length, with n = 2 exhibiting shorter $T_{1\rho}$ values than n = 3, 4, and 5; $T_{1\rho}$ increased with the increasing length of the CH_2 chain, indicating that the energy transfer was not easy. The difference in $T_{1\rho}$ values was mainly attributed to the cation length, with the shorter (n = 2) length exhibiting a smaller value, owing to the presence of paramagnetic Cu^{2+} ions. ^1H $T_{1\rho}$ values are very short after the inclusion of paramagnetic ions. The Cu^{2+} ions in $[NH_3(CH_2)_nNH_3]CuCl_4$, which are paramagnetic and bonded with the inorganic layer through N–H···Cl hydrogen bonds, directly affected the ^1H environment. With respect to the 2D structure of solar cell materials, the applicability of organic-inorganic hybrid compounds can be confirmed more clearly by knowing the energy transfer for a molecular motion for the spin-lattice relaxation times $T_{1\rho}$ along the length of a cation.

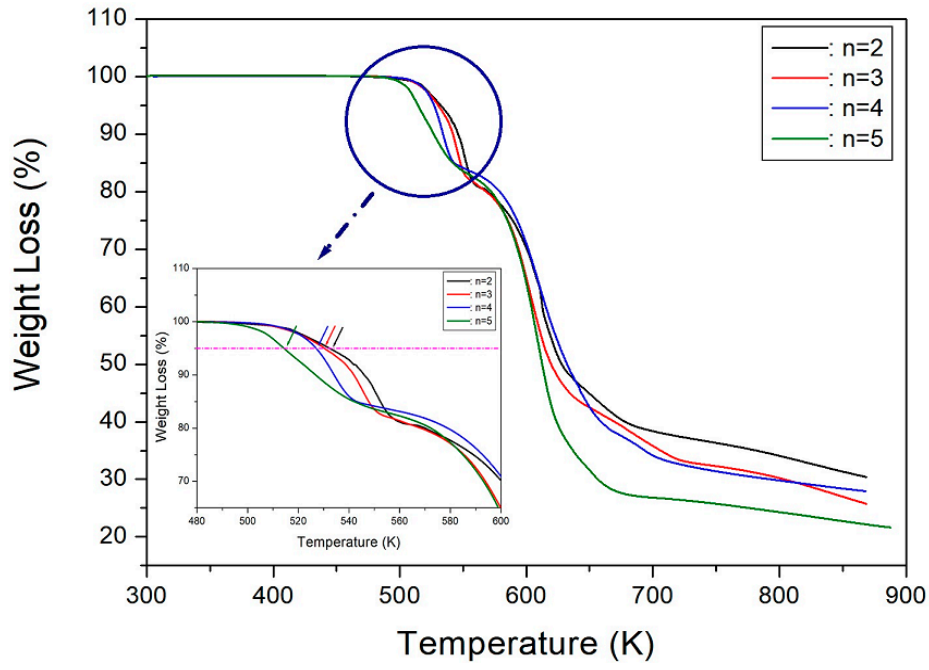

Figure 9. TGA curves of $[NH_3(CH_2)_nNH_3]CuCl_4$ (n = 2, 3, 4, and 5) (inset: expansion of TGA curves near T_d).

4. Materials and Methods

$[NH_3(CH_2)_5NH_3]CuCl_4$ single crystals were grown by gradually evaporating an aqueous solution of $NH_2(CH_2)_5NH_2{\cdot}2HCl$ (Aldrich, 98%) and $CuCl_2$ (Aldrich, 97%) at a constant temperature of 300 K. The grown single crystals that were $3 \times 3 \times 1.5$ mm in size exhibited a yellow color.

The XRD powder pattern experiments of the $[NH_3(CH_2)_5NH_3]CuCl_4$ crystal at several temperatures were measured in the measuring 2θ of 5–60° using an XRD system equipped with a Mo-Kα radiation source. The lattice parameters at various temperatures were determined by single-crystal X-ray diffraction (XRD) at the Seoul Western Center of the Korea Basic Science Institute (KBSI). A crystal block was picked up with paratone oil and mounted on a Bruker D8 Venture PHOTON III M14 diffractometer equipped with a graphite-monochromated Mo-Kα radiation source. Data were collected and integrated using SMART APEX3 (Bruker, 2016) and SAINT (Bruker, 2016). The absorption was corrected by a multi-scan method implemented in SADABS. The structure was solved using direct methods and refined by full-matrix least-squares on F^2 using SHELXTL. All non-hydrogen atoms were refined anisotropically, and the hydrogen atoms were added to their geometrically ideal positions.

TGA and DTA experiments were performed in the temperature range of 300–873 K on a thermogravimetric analyzer (TA Instruments) at a heating rate of 10 K/min with an N_2 gas flow [42]. Additionally, a twin domain pattern, observed in the 300–680 K temperature range, was measured using an optical polarizing microscope by placing the prepared single crystals on a Linkam THM-600 heating stage.

NMR chemical shifts and spin-lattice relaxation times ($T_{1\rho}$) for ^1H and ^{13}C in $[NH_3(CH_2)_5NH_3]CuCl_4$ crystals were measured using a Bruker 400 MHz Avance II+ solid-state NMR spectrometer at the same facility, KBSI. The Larmor frequency was $\omega_o/2\pi$ = 400.13 MHz for ^1H NMR, and $\omega_o/2\pi$ = 100.61 MHz for ^{13}C NMR. To minimize the spinning sideband, the sample tube spinning speed was set to 10 kHz, and TMS was used as reference material to accurately measure the NMR chemical shifts. $T_{1\rho}$ values were obtained using a $\pi/2-\tau$ pulse, followed by a spin-lock pulse of duration τ, and the width of the $\pi/2$ pulse for ^1H and ^{13}C was in the 3.2–3.9 μs range. The temperature was changed by adjusting the N_2 gas flow and the heater current, and the NMR experiment was conducted in the 180–430 K temperature range.

5. Conclusions

We discussed XRD, TGA, and NMR experiments to investigate the crystal structure, thermal stabilities, and physical properties of $[NH_3(CH_2)_5NH_3]CuCl_4$ crystal. First, the monoclinic structure and lattice parameter were confirmed by XRD, and its thermodynamic property was observed at about 514 K without phase transition. NMR analysis indicated that the crystallographic environment of ^1H in NH_3 and that of ^{13}C on C3, located close to NH_3 at both ends of the cation, were changed, indicating a large structural change of $CuCl_4$ connected to the N–H···Cl. The effects of the length of CH_2 in the cation on the molecular motions and thermal properties will facilitate future research on their potential application in the research of environment-friendly hybrid perovskite solar cells.

Author Contributions: A.R.L. designed the project and wrote the manuscript. S.H.P. prepared the samples and performed DSC and TGA experiments. All authors have read and agreed to the published version of the manuscript.

Funding: This research was supported by the Basic Science Research Program of the National Research Foundation of Korea (NRF), funded by the Ministry of Education, Science, and Technology (2018R1D1A1B07041593 and 2016R1A6A1A03012069).

Data Availability Statement: Not applicable.

Conflicts of Interest: The authors declare no conflict of interest.

Sample Availability: Samples of the compounds are available from the authors.

References

1. Rao, C.N.R.; Cheetham, A.K.; Thirumurugan, A. Hybrid inorganic-organic materials: A new family in condensed matter physics. *J. Phys. Condens. Matter.* **2008**, *20*, 83202. [CrossRef]
2. Cheng, Z.; Lin, J. Layered organic-inorganic hybrid perovskites: Structure, optical properties, film preparation, patterning and templating engineering. *Cryst. Eng. Com.* **2010**, *12*, 2646–2662. [CrossRef]
3. Mostafa, M.F.; El-khiyami, S.S. Crystal structure and electric properties of the organic-inorganic hybrid: $[(CH_2)_6(NH_3)_2]ZnCl_4$. *J. Solid State Chem.* **2014**, *209*, 82–88. [CrossRef]
4. Chen, Q.; Marco, N.D.; Yang, Y.; Song, T.-B.; Chen, C.-C.; Zhao, H.; Hong, Z.; Zhou, H.; Yang, Y. Under the spotlight: The organic–inorganic hybrid halide perovskite for optoelectronic applications. *Nano Today* **2015**, *10*, 355–396. [CrossRef]
5. Abdel-Aal, S.K.; Abdel-Rahman, A.S.; Kocher-Oberlehner, G.G.; Ionov, A.; Mozhchil, R. Structure, optical studies of 2D hybrid perovskite for photovoltaic applications. *Acta Cryst. A* **2017**, *70*, C1116. [CrossRef]
6. Liu, Y.; Collins, L.; Proksch, R.; Kim, S.; Watson, B.R.; Doughty, B.; Calhoun, T.R.; Ahmadi, M.; Ievlev, A.V.; Jesse, S.; et al. Chemical nature of ferroelastic twin domains in $CH_3NH_3PbI_3$ perovskite. *Nat. Mater.* **2018**, *17*, 1013–1019. [CrossRef]
7. Lee, J.; Lee, W.; Kang, K.; Lee, T.; Lee, S.K. Layer-by-Layer Structural Identification of 2D Ruddlesden–Popper Hybrid Lead Iodide Perovskites by Solid-State NMR Spectroscopy. *Chem. Mater.* **2021**, *33*, 370–377. [CrossRef]
8. Asaji, T.; Ito, Y.; Seliger, J.; Zagar, V.; Gradisek, A.; Apih, T. Phase transition and ring-puckering motion in a metal-organic perovskite $[(CH_2)_3NH_2][Zn(HCOO)_3]$. *J. Phys. Chem. C* **2012**, *116*, 12422. [CrossRef]
9. Asaji, T.; Ashitomi, K. Phase transition and cationic motion in a metal-organic perovskite, dimethylammonium zinc formate $[(CH_3)_2NH_2][Zn(HCOO)_3]$. *J. Phys. Chem. C* **2013**, *117*, 10185. [CrossRef]
10. Simenas, M.; Ciupa, A.; Maczka, M.; Poppl, A.; Banys, J. EPR study of structural phase transition in manganese-doped $[(CH_3)_2NH_2][Zn(HCOO)_3]$ metal-organic framework. *J. Phys. Chem. C* **2015**, *119*, 24522. [CrossRef]
11. Abhyankar, N.; Kweon, J.J.; Orio, M.; Bertaina, S.; Lee, M.; Choi, E.S.; Fu, R.; Dalal, N.S. Understanding ferroelectricity in the Pb-free perovskite-like metal-organic framework $[(CH_3)_2NH_2]Zn(HCOO)_3$: Dielectric, 2D NMR, and theoretical studies. *J. Phys. Chem. C* **2017**, *121*, 6314. [CrossRef]
12. Simenas, M.; Balciunas, S.; Trzebiatowska, M.; Ptak, M.; Maczka, M.; Volkel, G.; Poppl, A.; Banys, J. Electron paramagnetic resonance and electric characterization of a $[CH_3NH_2NH_2][Zn(HCOO)_3]$ perovskite metal formate framework. *J. Mater. Chem. C* **2017**, *5*, 4526. [CrossRef]
13. Simenas, M.; Balciunas, S.; Ciupa, A.; Vilciauskas, L.; Jablonskas, D.; Kinka, M.; Sieradzki, A.; Samulionis, V.; Maczka, M.; Banys, J. Elucidation of dipolar dynamics and the nature of structural phases in the $[(CH_3)_2NH_2][Zn(HCOO)_3]$ hybrid perovskite framework. *J. Mater. Chem. C* **2019**, *7*, 6779. [CrossRef]
14. Simenas, M.; Ptak, M.; Khan, A.H.; Dagys, L.; Balevicius, V.; Bertmer, M.; Volkel, G.; Maczka, M.; Poppl, A.; Banys, J. Spectro scopic study of $[(CH_3)_2NH_2][Zn(HCOO)_3]$ hybrid perovskite containing different nitrogen isotopes. *J. Phys. Chem. C* **2018**, *122*, 10284. [CrossRef]
15. Gonzalez-Carrero, S.; Galian, R.E.; Perez-Prieto, J. Organometa halide perovskites: Bulk low-dimension materials and nanoparticles. *Part. Syst. Charact.* **2015**, *32*, 709–720. [CrossRef]
16. Mostafa, M.F.; Elkhiyami, S.S.; Alal, S.A. Discontinuous transition from insulator to semiconductor induced by phase change of the new organic-inorganic hybrid $[(CH_2)_7(NH_3)_2]CoBr_4$. *Mat. Chem. Phys.* **2017**, *199*, 454–463. [CrossRef]
17. Abdel-Aal, S.K. Synthesis, characterization, thermal, and electric properties of new diammonium hybrid perovskite $[NH_3\text{-}(CH_2)_7\text{-}NH_3]CaCl_2Br_2$. *Solid State Ion.* **2017**, *303*, 29–36. [CrossRef]
18. Abdel-Adal, S.K.; Kocher-Oberlehner, G.; Ionov, A.; Mozhchil, R.N. Effect of organic chain length on structure, electronic composition, lattice potential energy, and optical properties of 2D hybrid perovskites $[(NH_3)(CH_2)_n(NH_3)]CuCl_4$, n = 2–9. *Appl. Phys. A* **2017**, *123*, 531. [CrossRef]
19. Liu, W.; Xing, J.; Zhao, J.; Wen, X.; Wang, K.; Peixiang, L.; Xiong, Q. Giant two-dimensional absorption and its saturation in 2D organic-inorganic perovskite. *Adv. Opt. Mater.* **2017**, *5*, 1601045. [CrossRef]
20. Mondal, P.; Abdel-Aal, S.K.; Das, D.; Manirul Islam, S.K. Catalytic activity of crystallographically characterized organic-inorganic hybrid containing 1,5-di-amino-pentane tetrachloro manganate with perovskite type structure. *Cat. Let.* **2017**, *147*, 2332–2339. [CrossRef]
21. Elseman, M.; Shalan, A.E.; Sajid, S.; Rashad, M.M.; Hassan, A.M.; Li, M. Copper-substituted lead perovskite materials constructed with different halides for working $(CH_3NH_3)_2CuX_4$-based perovskite solar cells from experimental and theoretical view. *ACS Appl. Mater. Interfaces* **2018**, *10*, 11699–11707. [CrossRef] [PubMed]
22. Aramburu, J.A.; Garcia-Fernandez, P.; Mathiesen, N.R.; Garcia-Lastra, J.M.; Moreno, M. Changing the usual interpretation of the structure and ground state of Cu^{2+} layered perovskites. *J. Phys. Chem. C* **2018**, *122*, 5071–5082. [CrossRef]
23. Pradeesh, K.; Yadav, G.S.; Singh, M.; Vijaya Prakash, G. Synthesis, structure and optical studies of inorganic-organic hybrid semiconductor, $NH_3(CH_2)_{12}NH_3PbI_4$. *Mater. Chem. Phys.* **2010**, *124*, 44–47. [CrossRef]
24. Saikumar, S.; Ahmad, J.J.; Baumberg, G.; Vijaya Prakash, G. Fabrication of excitonic luminescent inorganic-organic hybrid nano- and microcrystals. *Scr. Mater.* **2012**, *67*, 834–837. [CrossRef]
25. Staskiewicz, B.; Czupinski, O.; Czapla, Z. On some spectroscopic properties of a layered 1,3-diammoniumpropylene tetrabromocadmate hybrid crystal. *J. Mol. Struct.* **2014**, *1074*, 723–731. [CrossRef]

26. Ahmad, S.; Hanmandlu, C.; Kanaujia, P.K.; Vijaya Prakash, G. Direct deposition strategy for highly ordered inorganic organic perovskite thin films and their optoelectric applications. *Opt. Mater. Express* **2014**, *4*, 1313–1323. [CrossRef]
27. Wang, Y.; Ji, C.; Liu, X.; Han, S.; Zhang, J.; Sun, Z.; Khan, A.; Luo, J. (1,4-Butyldiammonium) $CdBr_4$: A layered organic–inorganic hybrid perovskite with a visible-blind ultraviolet photoelectric response. *Inorg. Chem. Front.* **2018**, *5*, 2450–2455. [CrossRef]
28. Czupinski, O.; Ingram, A.; Kostrzewa, M.; Przeslawski, J.; Czapla, Z. On the Structural phase transition in a perovskite-type diaminopropanetetrachlorocuprate(II) $NH_3(CH_2)_3NH_3CuCl_4$ crystal. *Acta Phys. Pol. A* **2017**, *131*, 304–310. [CrossRef]
29. Liang, D.; Lian, X.; Li, X.; Luo, B. Pb alloying enables efficient broadband emission of two dimensional $[NH_3(CH_2)_4NH_3]CdBr_4$. *J. Solid State Chem.* **2021**, *293*, 121772. [CrossRef]
30. Przeslawski, J.; Czapla, Z.; Crofton, M.; Dacko, S. On the "inverted" phase transitions in ferroic crystals containing propylenediammonium cations. *Ferroelectrics* **2018**, *534*, 220–227. [CrossRef]
31. Svane, K.L.; Forse, A.C.; Grey, C.P.; Kieslich, G.; Cheetham, A.K.; Walsh, A.; Butler, A.K. How Strong Is the Hydrogen Bond in Hybrid Perovskites? *J. Phys. Chem. Lett.* **2017**, *8*, 6154–6159. [CrossRef] [PubMed]
32. Zang, W.; Xiong, R.G. Ferroelectric metal-organic frameworks. *Chem. Rev.* **2012**, *112*, 1163–1195. [CrossRef] [PubMed]
33. Lim, A.R.; Kim, S.H. Physicochemical property investigations of perovskite-type layer crystals $[NH_3(CH_2)_nNH_3]CdCl_4$ (n = 2, 3, and 4) as a function of length n of CH_2. *ACS Omega* **2021**, *6*, 27568–27577. [CrossRef] [PubMed]
34. Correa-Baena, J.-P.; Saliba, M.; Buonassisi, T.; Gratzel, M.; Abate, A.; Tress, W.; Hagfeldt, A. Promises and Challenges of Perovskite Solar Cells. *Science* **2017**, *358*, 739–744. [CrossRef]
35. Lin, K.; Xing, J.; Quan, L.N.; de Arquer, F.P.G.; Gong, X.; Lu, J.; Xie, L.; Zhao, W.; Zhang, D.; Yan, C. Perovskite light-emitting diodes with external quantum efficiency exceeding 20 percent. *Nature* **2018**, *562*, 245–248. [CrossRef]
36. Akkerman, Q.A.; Manna, L. What defines a halide perovskite? *ACS Energy Lett.* **2021**, *6*, 1803. [CrossRef]
37. Kind, R.; Plesko, S.; Gunter, P.; Roos, J.; Fousek, J. Structural phase transitions in the perovskite-type layer compounds $NH_3(CH_2)_3NH_3CdCl_4$, $NH_3(CH_2)_4NH_3MnCl_4$, and $NH_3(CH_2)_5NH_3CdCl_4$. *Phys. Rev. B* **1981**, *23*, 5301. [CrossRef]
38. Garland, J.K.; Emerson, K.; Pressprich, M.R. Structures of four- and five carbon alkyldiammonium tetrachlorocuprate (II) and tetrabromocuprate (II) salts. *Acta Cryst. C* **1990**, *46*, 1603–1609. [CrossRef]
39. Filloleau, N.; Zouari, R.; Bissey, J.-C.; Chanh, N.B.; Daoud, A. EPR study of the two-dimensional molecular composite $[NH_3(CH_2)_5NH_3]CuCl_4$: Evidence for both spin diffusion and spin anisotropies. *Appl. Magn. Reson.* **1998**, *14*, 25–35. [CrossRef]
40. von Kanel, H. Magnetic and optical properties of the layer type magnets $(CH_2)_2(ND_3)_2MnCl_4$ and $(CH_2)_n(NH_3)_2CuCl_4$, n = 2, 3, 5. *Phys. B* **1979**, *96*, 167–193. [CrossRef]
41. Lim, A.R. Dynamics of $NH_3(CH_2)_2NH_3$ cation in perovskite layer crystal $NH_3(CH_2)_2NH_3CuCl_4$ by M. *Solid State Commun.* **2020**, *312*, 113862. [CrossRef]
42. Yoon, M.B.; Lee, W.J.; Lim, A.R. Thermal property and structural molecular dynamics of organic-inorganic hybrid perovskite 1,4-butane diammonium tetrachlorocuprate. *RSC Adv.* **2020**, *10*, 34800–34805. [CrossRef] [PubMed]
43. Lim, A.R. Structural characterization, thermal properties, and molecular motions near the phase transition in hybrid perovskite $[(CH_2)_3(NH_3)_2]CuCl_4$ crystals:^{1}H, ^{13}C, and ^{14}N nuclear magnetic resonance. *Sci. Rep.* **2020**, *10*, 20853. [CrossRef]
44. Mostafa, M.F.; Hassen, A. Phase transition and electric properties of long chain Cd(II) layered perovskite. *Phase Transit.* **2006**, *79*, 305–321. [CrossRef]
45. Khechoubi, M.; Bendani, A.; Chanh, N.B.; Courseille, C.; Duplessix, R.; Couzi, M. Thermal conformational changes in a bidimensional molecular composite material: A thermodynamic and crystallographic study of NH_3-$(CH_2)_4$-NH_3 $CdCl_4$. *J. Phys. Chem. Solids* **1994**, *55*, 1277–1288. [CrossRef]
46. Mostafa, M.F.; El-hakim, S.A. Structural phase transition and the dielectric permittivity of the model lipid bilayer $[(CH_2)_{12}(NH_3)_2]CuCl_4$. *Phase Transit.* **2003**, *76*, 587–599. [CrossRef]
47. Mostafa, M.F.; Youssef, A.A.A. Magnetic and electric studies of a new Cu(II) perovskite-like material. *Z. Naturforsch.* **2004**, *59*, 35–46. [CrossRef]
48. Anbarasan, R.; Eniya, P.; Lakshmi, M.A.; Sundar, J.K. Structural, spectal, optical, thermal and quantum chemical investigations on ethylenediammonium tetrachloro zinc crystal for optoelectric appications. *J. Mol. Struct.* **2019**, *1188*, 165–172. [CrossRef]
49. Herms, I.M.; Bretschneider, S.A.; Bergmann, V.W.; Li, D.; Klasen, A.; Mars, J.; Tremel, W.; Laquai, F.; Butt, H.-J.; Mezger, M.; et al. Ferroelastic fingerprints in methylammonium lead iodide perovskite. *J. Phys. Chem. C* **2016**, *120*, 5724–5731. [CrossRef]
50. Strelcov, E.; Dong, Q.; Li, T.; Chae, J.; Shao, Y.; Deng, Y.; Gruverman, A.; Huang, J.; Centrone, A. $CH_3NH_3PbI_3$ perovskites: Ferroelasticity revealed. *Sci. Adv.* **2017**, *3*, e1602165. [CrossRef]
51. Maczka, M.; Ptak, M.; Vasconcelos, D.L.M.; Giriunas, L.; Freire, P.T.C.; Bertmer, M.; Banys, J.; Simenas, M. NMR and raman scattering studies of temperature- and pressure-driven phase transitions in $CH_3NH_2NH_2PbCl_3$ perovskite. *J. Phys. Chem. C* **2020**, *124*, 26999. [CrossRef]
52. Abragam, A. *The Principles of Nuclear Magnetism*; Oxford University Press: Oxford, UK, 1961.
53. Harris, R.K. *Nuclear Magnetic Resonance Spectroscopy*; Pitman Pub.: London, UK, 1983.
54. Koenig, J.L. *Spectroscopy of Polymers*; Elsevier: New York, NY, USA, 1999.